

21. V. Randle, *Scr. Mater.* **54**, 1011 (2006).
 22. S. R. Ortner, *Acta Metall. Mater.* **39**, 341 (1991).
 23. Y. Z. Huang, J. M. Titchmarsh, *Acta Mater.* **54**, 635 (2006).
 24. A.K. and G.J. wish to acknowledge funding received from the Engineering and Physical Sciences Research Council (U.K.). W.L. also acknowledges additional

support received from the Danish National Research Foundation.

Supporting Online Material

www.sciencemag.org/cgi/content/full/321/5887/382/DC1
 Materials and Methods

Measurement of the Elastic Properties and Intrinsic Strength of Monolayer Graphene

Changgu Lee,^{1,2} Xiaoding Wei,¹ Jeffrey W. Kysar,^{1,3} James Hone^{1,2,4*}

We measured the elastic properties and intrinsic breaking strength of free-standing monolayer graphene membranes by nanoindentation in an atomic force microscope. The force-displacement behavior is interpreted within a framework of nonlinear elastic stress-strain response, and yields second- and third-order elastic stiffnesses of 340 newtons per meter (N m^{-1}) and -690 N m^{-1} , respectively. The breaking strength is 42 N m^{-1} and represents the intrinsic strength of a defect-free sheet. These quantities correspond to a Young's modulus of $E = 1.0$ terapascals, third-order elastic stiffness of $D = -2.0$ terapascals, and intrinsic strength of $\sigma_{\text{int}} = 130$ gigapascals for bulk graphite. These experiments establish graphene as the strongest material ever measured, and show that atomically perfect nanoscale materials can be mechanically tested to deformations well beyond the linear regime.

In 1921, Griffith published a groundbreaking study on the fracture of brittle materials that established the relationship between the change of potential energy of a brittle system with crack growth and the free energy of a newly created surface (1). As a result of this insight, Griffith deduced that the actual breaking strength of a brittle material is governed by the sizes of defects and flaws within the material, rather than the intrinsic strength of its atomic bonds. To emphasize the point, Griffith wrote that “in the limit, in fact, a fiber consisting of a single line of molecules must possess the theoretical molecular tensile strength,” the maximum stress that can be supported by the material prior to failure in a pristine material without defects, here denoted as the intrinsic strength. He then proceeded to experimentally estimate the intrinsic tensile strength by measuring the breaking strength of a series of glass fibers with progressively smaller diameters and extrapolating the results to an atomic radius. He extrapolated an intrinsic strength of about $E/9$, where E is the elastic stiffness (Young's modulus) of the material under uniaxial tension. The concepts related to fracture have been well developed in the intervening decades; however, a direct and repeatable measurement of the in-

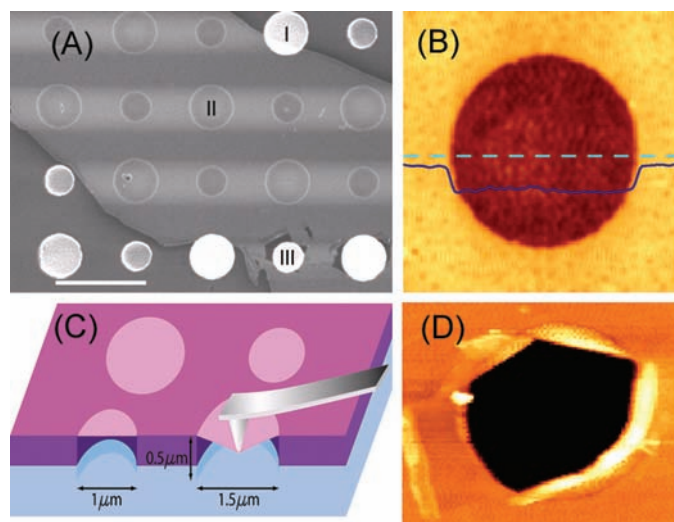
trinsic breaking strength of a material has remained elusive. We probed the intrinsic strength of monolayer graphene, as well as its linear and nonlinear elastic properties.

Graphene, which consists of a two-dimensional (2D) sheet of covalently bonded carbon atoms, forms the basis of both 3D graphite and 1D carbon nanotubes. Its intrinsic strength, predicted to exceed that of any other material (2), motivates the use of carbon-fiber reinforcements in advanced composites, and may permit such exotic structures as a “space elevator” if macroscopic fibers close to the theoretical strength can be realized. However, the intrinsic strength of this material has still not been definitively measured

because of the inevitable presence of defects and grain boundaries in macroscopic samples. In the past few years, multiple studies (3–10) of carbon nanotubes have confirmed their high stiffness and strength. However, determination of these quantities has been difficult because of uncertainty in the sample geometry, stress concentration at clamping points, structural defects, and unknown load distribution among shells in multiwalled nanotubes. Recent experimental advances (11) now permit the study of individual graphene sheets. We used atomic force microscope (AFM) nanoindentation to measure the mechanical properties of monolayer graphene membranes suspended over open holes. This technique has recently been used to study multilayer graphene (12, 13) and offers three important advantages over experiments on nanotubes: The sample geometry can be precisely defined, the 2D structure is less sensitive to the presence of a single defect, and the sheet is clamped around the entire hole circumference, as opposed to two points in the case of nanotubes.

For this study, a 5-by-5-mm array of circular wells (diameters 1.5 μm and 1 μm , depth 500 nm) was patterned onto a Si substrate with a 300-nm SiO_2 epilayer by nanoimprint lithography and reactive ion etching (Fig. 1). Graphite flakes were then mechanically deposited onto the substrate (14). Optical microscopy was used to find flakes of monolayer graphene, whose thicknesses were confirmed with Raman spectroscopy (15) (fig. S1). Figure 1A shows a monolayer flake deposited over many circular wells to form a series of free-standing membranes. Noncontact mode AFM imaging (Fig. 1B) confirmed that the

Fig. 1. Images of suspended graphene membranes. (A) Scanning electron micrograph of a large graphene flake spanning an array of circular holes 1 μm and 1.5 μm in diameter. Area I shows a hole partially covered by graphene, area II is fully covered, and area III is fractured from indentation. Scale bar, 3 μm . (B) Noncontact mode AFM image of one membrane, 1.5 μm in diameter. The solid blue line is a height profile along the dashed line. The step height at the edge of the membrane is about 2.5 nm. (C) Schematic of nanoindentation on suspended graphene membrane. (D) AFM image of a fractured membrane.



¹Department of Mechanical Engineering, Columbia University, New York, NY 10027, USA. ²Defense Advanced Research Projects Agency Center for Integrated Micro/Nano-Electromechanical Transducers (iMINT), Columbia University, New York, NY 10027, USA. ³Center for Nanostructured Materials, Columbia University, New York, NY 10027, USA. ⁴Center for Electronic Transport in Molecular Nanostructures, Columbia University, New York, NY 10027, USA.

*To whom correspondence should be addressed. E-mail: jh2228@columbia.edu

graphene membranes were stretched tautly across the well openings. It also revealed that the graphene adheres to the vertical wall of the hole for 2 to ~10 nm, presumably because of van der Waals attraction to the substrate.

The mechanical properties of the free-standing films were probed by indenting the center of each film with an AFM (XE-100, Park Systems), as illustrated in Fig. 1C. Because of the strength of the films, cantilevers with diamond tips were used for this study. Two different cantilevers were used, with tip radii of 27.5 and 16.5 nm, as measured before and after indentation via transmission electron microscopy (TEM) (fig. S2). The corresponding cantilever spring constants were calibrated against a reference cantilever (16). Prior to indenting, the graphene membranes were scanned in a noncontact AFM mode and the AFM tip was subsequently positioned to within 50 nm of the center. Mechanical testing was performed at a constant displacement rate, followed by load reversal. This cycle was repeated several times for each film tested. The data showed no hysteresis, which demonstrated the elastic behavior of the film and showed that the graphene film did not slip around the periphery of the well. The force-displacement measurements were highly repeatable; data sets from different flakes, membrane diameters, displacement rates, and indenter tip radii yielded values of the elastic modulus that were statistically indistinguishable. Once the data for elastic properties of the films were recorded, the films were once again indented at the same rate, but this time to failure. The force-displacement data were processed to determine the elastic properties and breaking stress of the graphene membranes. Full details of the experimental procedure and data analysis can be found in (16).

The elastic response of the graphene must be considered nonlinear because the stress-strain response must curve over to a maximum point that defines the intrinsic breaking stress. An elastic (i.e., reversible) response implies the existence of an energy potential that is a function of strain that can be expressed as a Taylor series in powers of strain. The lowest-order (quadratic) term leads to linear elastic response. The

third-order term gives rise to nonlinear elastic behavior (17). The resulting isotropic elastic response under uniaxial extension can be expressed as

$$\sigma = E\varepsilon + D\varepsilon^2 \quad (1)$$

where σ is the symmetric second Piola-Kirchhoff stress, ε is the uniaxial Lagrangian strain, E is the Young's modulus, and D is the third-order elastic modulus. The value of D is typically negative, so the presence of the second-order term leads to a lessening of stiffness at high tensile strains and an increasingly stiff response at high compressive strains. E was determined from components of the second-order fourth-rank stiffness tensor (with two independent components for an isotropic material), whereas D was determined from components of both the second-order fourth-rank stiffness tensor and the third-order sixth-rank stiffness tensor (with three independent components for an isotropic material). Numerical simulations of graphene sheets and nanotubes suggest that a nonlinear elastic response is appropriate (18, 19).

This thermodynamically rigorous nonlinear form of the stress-strain response should capture the salient features of the elastic behavior of graphene. The maximum of the elastic stress-strain response defines the intrinsic stress, which for this functional form is $\sigma_{\text{int}} = -E^2/4D$ at the strain $\varepsilon_{\text{int}} = -E/2D$, so it remains only to determine E and D from the experimental results. We determined the value of E based on the experimental force-displacement data and inferred the value of D from the experimental breaking force.

Monolayer graphene is a true 2D material, so its strain energy density is normalized by the area of the graphene sheet rather than by the volume. Therefore, its behavior under tensile loading is properly described by a 2D stress σ^{2D} and elastic constants E^{2D} and D^{2D} with units of force/length. The equations given above are valid for any dimensionality. For purposes of comparison to bulk graphite and other materials, these quantities can be divided by the interlayer spacing in graphite [$h = 0.335$ nm (20)] in order to obtain the corresponding 3D parameters. How-

ever, the derived quantities are not intrinsic properties of the single sheet and cannot be used to predict other mechanical properties, such as bending stiffness (21).

Even at the maximum curvatures present in these experiments, the energy from bending the graphene membrane is three orders of magnitude smaller than the energy from in-plane strain, using *ab initio* values for the in-plane stiffness and flexural rigidity (22). Therefore, the graphene can be modeled as a 2D membrane (i.e., it has zero bending stiffness). We performed detailed finite-element analyses for this geometry and loading based on the constitutive relations in Eq. 1, using various values of D^{2D} , tip radius, and indenter position (16). Three important points emerged from this analysis. First, the resulting force-displacement curve made by using the nonlinear elastic model was virtually indistinguishable from that of the linear model (where $D^{2D} = 0$). The calculated radial stress distribution and shape of the deformed film (Fig. 2B) show why nonlinear effects can be ignored while simulating the force-displacement response: Even close to breaking, at most 1% of the graphene film is strained to the point where the nonlinear term in Eq. 1 becomes important. Second, the simulations demonstrated that the force-displacement curve is insensitive to the indenter tip radius when $R \ll a$, where R is the tip radius and a is the membrane diameter. Third, the force-displacement response is insensitive to the position of the tip (to within experimental uncertainty) if the indenter tip is located within $a/10$ of the center of the film. Therefore, for the purposes of modeling the force-displacement behavior, the system can be approximated as a clamped circular membrane, made of a linear isotropic elastic material, under central point loading. Isotropic mechanical properties were used because the graphene atomic lattice has sixfold rotation symmetry (23).

Given the above model, the force-displacement behavior can be approximated (16, 24, 25) as

$$F = \sigma_0^{2D}(\pi a) \left(\frac{\delta}{a} \right) + E^{2D}(q^3 a) \left(\frac{\delta}{a} \right)^3 \quad (2)$$

where F is applied force, δ is the deflection at the center point, σ_0^{2D} is the pretension in the film, ν is Poisson's ratio [taken here as 0.165, the Poisson's ratio for graphite in the basal plane (26)], and $q = 1/(1.05 - 0.15\nu - 0.16\nu^2) = 1.02$ is a dimensionless constant. The solid line in Fig. 2A shows the least-squares curve fit of one set of experimental data, based on Eq. 2, taking σ_0^{2D} and E^{2D} as free parameters. The closeness of the fit further validates the appropriateness of this model.

For this study, membranes from two separate graphene flakes were tested. These included seven with 1- μm diameters and six with 1.5- μm diameters from flake 1, and five of each size from flake 2. Each flake was probed using a different cantilever. For each membrane, approximately three loading/unloading curves were collected,

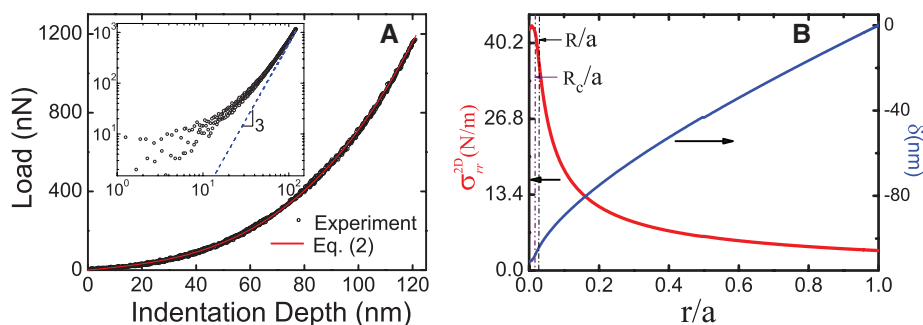


Fig. 2. (A) Loading/unloading curve and curve fitting to Eq. 2. The curve approaches cubic behavior at high loads (inset). (B) Maximum stress and deflection of graphene membrane versus normalized radial distance at maximum loading (simulation based on nonlinear elastic behavior in Eq. 1). The dashed lines indicate the tip radius R and contact radius R_c .

to multiple depths (between 20 and 100 nm). In total, 67 values of σ_0^{2D} and E^{2D} were determined by fitting to Eq. 2. Figure 3A shows the distribution of the derived values of E^{2D} . The mean value of E^{2D} is 342 N m^{-1} , with a standard deviation of 30 N m^{-1} . An estimate of the overall uncertainty in the measured value is discussed in (16). The elastic modulus values obtained from all data subsets (different flakes, tips, well radii, indentation depth, and indentation speed) were statistically indistinguishable.

Figure 3B shows the derived values for the film pretension, which range from 0.07 to 0.74 N m^{-1} , with flake 2 showing larger pretension on average. These values are remarkably high, higher than the fracture strengths of many conventional materials. We also observed that, because the membrane follows the wall for 2 to 10 nm, the actual membrane profile is ~ 0.2 to 1% longer than the nominal well diameter. This elongation would lead to an added stress of 0.7 to 3.4 N m^{-1} , larger than the measured pretension in most cases. Therefore, we conclude that the graphene is nominally in a compressed state when not suspended.

The intrinsic strength of graphene was measured by loading the membranes to the breaking point. Figure 4A shows four typical breaking curves, for both tip radii and well diameters. There is no sign of slippage or other irreversible deformation prior to catastrophic failure. Figure 1D shows an AFM image of a fractured membrane. The graphene film still hangs around the edge of the hole, which suggests that fracture started at the indentation point. The films break at large deflections (above 100 nm) and forces of about $1.8 \mu\text{N}$ and $2.9 \mu\text{N}$ for the smaller and larger indenter tips, respectively. These forces were large enough to break standard Si AFM tips; TEM inspection confirmed that the diamond tips used in this study were not damaged. From those four typical curves, a clear pattern emerges: The force-displacement behavior is insensitive to tip radius, but the breaking force is mainly a function of tip radius and shows no dependence on membrane size, because of the extreme stress concentration (see also Fig. 2B) under the indenter tip.

The maximum stress for a clamped, linear elastic, circular membrane under a spherical

indenter as a function of applied load has been derived on the basis of a continuum model as

$$\sigma_m^{2D} = \left(\frac{FE^{2D}}{4\pi R} \right)^{\frac{1}{2}} \quad (3)$$

where σ_m^{2D} is the maximum stress at the central point of the film (27). This analytical solution helps illuminate the relationship among breaking force, tip radius, and maximum stress, in particular showing that the breaking force should vary inversely with tip radius. Analyzing all of the measured data using Eq. 3 yields an average breaking strength of 55 N m^{-1} . However, because the model ignores nonlinear elasticity, this value overestimates the strength.

The breaking forces we measured in the graphene films strongly suggest that the films in the neighborhood of the tip are free of defects, so that the maximum stress in the film represents the intrinsic strength. Two observations support this argument. First, the magnitude of the stresses under the indenter tip that we observed is consistent with predictions of intrinsic strength based on *ab initio* calculations for monolayer graphene (18, 19). Second, the distribution of breaking forces, as shown in Fig. 4B, was relatively narrow, whereas for brittle fracture one would expect a wider distribution depending on the random size, number, and position of defects under the tip. The second argument can be quantified by fitting the histograms to the Weibull distribution (28), which characterizes the failure of brittle materials with random defects (fig. S8). The statistics suggest that the material is defect-free, at least under the indenter tip. This is consistent with scanning tunneling microscopy measurements (29) of graphene films (from the same source material) that show no defects over regions of hundreds of square nanometers. Therefore, we used a nonlinear elastic model to treat the breaking force data as corresponding to the intrinsic strength of the graphene.

A series of numerical simulations was performed for the $1\text{-}\mu\text{m}$ -diameter graphene film and the 16.5-nm -radius indenter tip to determine the relationship between the indentation breaking force and the third-order elastic constant, D^{2D} . In each simulation, the breaking force was determined as that load at which the solution could no longer converge to an equilibrium state under the indenter tip because of the negative slope of the elastic response at strains larger than ϵ_{int} . The mean experimentally determined breaking force of 1770 nN was consistent with a value of $D^{2D} = -690 \text{ N m}^{-1}$. This value of D^{2D} was then used in the numerical model for the $1\text{-}\mu\text{m}$ -diameter graphene film and the 27.5-nm -radius indenter. The simulation predicted a breaking force (2880 nN) virtually identical to the mean experimental value of 2890 nN . Therefore, the experimentally determined values of the second-order and third-order elastic stiffnesses for monolayer graphene are $E^{2D} = 340 \pm 50 \text{ N m}^{-1}$

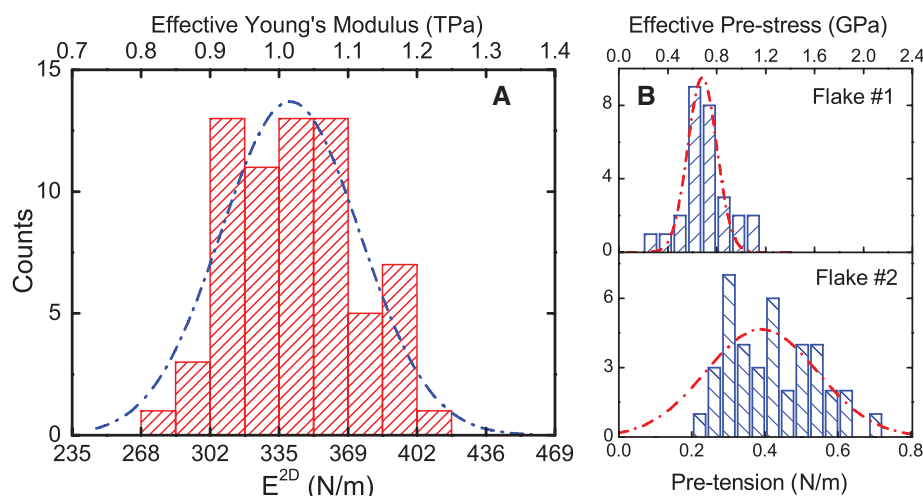


Fig. 3. Elastic response test results. (A) Histogram of elastic stiffness. (B) Histogram of film pretensions. Dashed lines in both plots represent Gaussian fits to data. The effective Young's modulus and prestress were obtained by dividing by the graphite interlayer spacing.

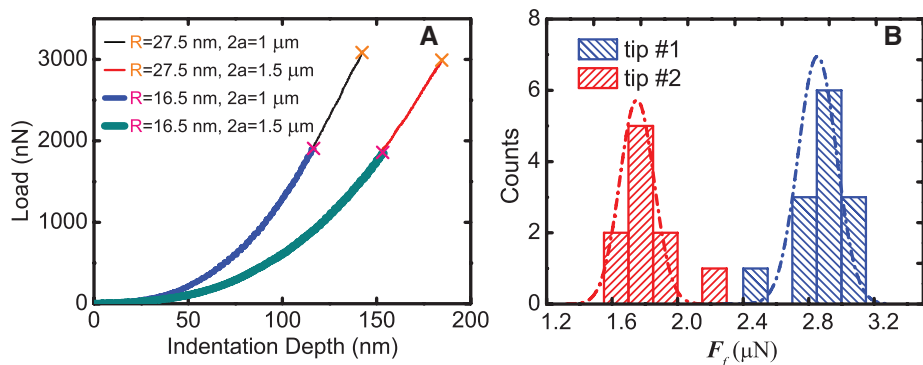


Fig. 4. Fracture test results. (A) Four typical tests, with different tip radii and film diameters; fracture loads are indicated by \times marks. Breaking force depended strongly on tip radius but not on sample diameter. (B) Histogram and Gaussian distribution of breaking force for both tips.

and $D^{2D} = -690 \pm 120 \text{ N m}^{-1}$, respectively. The intrinsic strength is $\sigma_{\text{int}}^{2D} = 42 \pm 4 \text{ N m}^{-1}$. These correspond to Young's modulus of $E = 1.0 \pm 0.1 \text{ TPa}$ and a third-order elastic stiffness of $D = -2.0 \pm 0.4 \text{ TPa}$, assuming an effective graphene thickness of 0.335 nm . The corresponding intrinsic stress is $\sigma_{\text{int}} = 130 \pm 10 \text{ GPa}$ at a strain of $\epsilon_{\text{int}} = 0.25$. Also, $\sigma_{\text{int}} \approx E/8$, which is very close to the value obtained by Griffith.

We compared our measured values with those from other experiments. Experiments on bulk graphite (26) yield $1.02 \pm 0.03 \text{ TPa}$ for the in-plane Young's modulus. Tensile tests (6–8) have been reported for both single-walled carbon nanotubes and multi-walled carbon nanotubes (MWCNTs). A broad range of stiffness values (0.27 TPa to 1.47 TPa) was obtained, with breaking strengths ranging from 3.6 to 63 GPa and failure strain up to 12% . An in situ tensile test (9) in a TEM reported intrinsic strength of $150 \pm 45 \text{ GPa}$ for a defect-free MWCNT. At least two recent experiments report mechanical tests performed on suspended graphene films; nanoindentation of suspended multilayer graphene flakes has been used to measure their bending stiffness (12) and extract a Young's modulus of 0.5 TPa (13). The elastic deformation and failure strength of graphene have been simulated using ab initio methods (18, 19). The predicted elastic response is highly nonlinear for strains above 10% and exhibits a maximum for pristine graphite between 118 and 121 GPa .

The intrinsic strength reported here serves as a benchmark for structural and mechanical

applications, although the strength of macroscopic graphitic materials is still limited by the presence of defects and grain boundaries. In addition, these measurements demonstrate that third-order elastic constants associated with nonlinear behavior can be measured in atomically perfect nanoscale materials. These measurements can be used to validate models of atomic potentials far beyond the linear regime.

References and Notes

- A. A. Griffith, *Philos. Trans. R. Soc. London Ser. A* **221**, 163 (1921).
- Q. Zhao, M. B. Nardelli, J. Bernholc, *Phys. Rev. B* **65**, 144105 (2002).
- A. Krishnan, E. Dujardin, T. W. Ebbesen, P. N. Yianilos, M. M. J. Treacy, *Phys. Rev. B* **58**, 14013 (1998).
- J. P. Salvetat *et al.*, *Phys. Rev. Lett.* **82**, 944 (1999).
- T. W. Tombler *et al.*, *Nature* **405**, 769 (2000).
- S. Xie, W. Li, Z. Pan, B. Chang, L. Sun, *J. Phys. Chem. Solids* **61**, 1153 (2000).
- M. F. Yu, B. S. Files, S. Arepalli, R. S. Ruoff, *Phys. Rev. Lett.* **84**, 5552 (2000).
- M. F. Yu *et al.*, *Science* **287**, 637 (2000).
- B. G. Demczyk *et al.*, *Mater. Sci. Eng. A* **334**, 173 (2002).
- B. I. Yakobson, P. Avouris, in *Carbon Nanotubes* (Springer-Verlag, Berlin, 2001), vol. 80, pp. 287–327.
- K. S. Novoselov *et al.*, *Proc. Natl. Acad. Sci. U.S.A.* **102**, 10451 (2005).
- M. Poot, H. S. J. v. d. Zant, *Appl. Phys. Lett.* **92**, 063111 (2008).
- I. W. Frank, D. M. Tanenbaum, A. M. Van der Zande, P. L. McEuen, *J. Vac. Sci. Technol. B* **25**, 2558 (2007).
- K. S. Novoselov *et al.*, *Proc. Natl. Acad. Sci. U.S.A.* **102**, 10451 (2005).
- A. C. Ferrari *et al.*, *Phys. Rev. Lett.* **97**, 187401 (2006).
- Materials and methods are available as supporting material on Science Online.
- R. N. Thurston, K. Brugger, *Phys. Rev.* **133**, A1604 (1964).
- F. Liu, P. M. Ming, J. Li, *Phys. Rev. B* **76**, 064120 (2007).
- R. Khare *et al.*, *Phys. Rev. B* **75**, 075412 (2007).
- R. Al-Jishi, G. Dresselhaus, *Phys. Rev. B* **26**, 4514 (1982).
- Y. Huang, J. Wu, K. C. Hwang, *Phys. Rev. B* **74**, 245413 (2006).
- B. I. Yakobson, C. J. Brabec, J. Bernholc, *Phys. Rev. Lett.* **76**, 2511 (1996).
- J. F. Nye, *Physical Properties of Crystals* (Oxford Univ. Press, New York, 1985).
- K. T. Wan, S. Guo, D. A. Dillard, *Thin Solid Films* **425**, 150 (2003).
- U. Komaragiri, M. R. Begley, *J. Appl. Mech.* **72**, 203 (2005).
- O. L. Blakslee, *J. Appl. Phys.* **41**, 3373 (1970).
- N. M. Bhatia, W. Nachbar, *Int. J. Non-Linear Mech.* **3**, 307 (1968).
- B. Lawn, *Fracture of Brittle Solids* (Cambridge Univ. Press, New York, ed. 2, 1993).
- E. Stolyarova *et al.*, *Proc. Natl. Acad. Sci. U.S.A.* **104**, 9209 (2007).
- We thank S. Berciaud for Raman spectroscopy of the graphene samples, Namiki Inc. for AFM cantilevers, and J. Hay and W. Oliver (MTS Nano Instruments) for useful interactions. We acknowledge support from NSF under awards CHE-0117752, CMMI-0500239, and DMR-0650555; iMINT (Award HR0011-06-1-0048); Air Force Office of Scientific Research grant FA9550-06-1-0214; and New York State Office of Science, Technology, and Academic Research. This work used shared experimental facilities supported primarily by the Materials Research Science and Engineering Center Program of NSF under award DMR-0213574, and the Cornell Nanoscale Science and Technology Facility, a member of the National Nanotechnology Infrastructure Network, which is supported by NSF (ECS-0335765).

Supporting Online Material

www.sciencemag.org/cgi/content/full/321/5887/385/DC1
Materials and Methods

Figs. S1 to S8

References

18 March 2008; accepted 11 June 2008

10.1126/science.1157996

Measurement of the Distribution of Site Enhancements in Surface-Enhanced Raman Scattering

Ying Fang,* Nak-Hyun Seong,* Dana D. Dlott†

On nanotextured noble-metal surfaces, surface-enhanced Raman scattering (SERS) is observed, where Raman scattering is enhanced by a factor, \bar{G} , that is frequently about one million, but underlying the factor \bar{G} is a broad distribution of local enhancement factors, η . We have measured this distribution for benzenethiolate molecules on a 330-nanometer silver-coated nanosphere lattice using incident light of wavelength 532 nm . A series of laser pulses with increasing electric fields burned away molecules at sites with progressively decreasing electromagnetic enhancement factors. The enhancement distribution $P(\eta)d\eta$ was found to be a power law proportional to $(\eta)^{-1.75}$, with minimum and maximum values of 2.8×10^4 and 4.1×10^{10} , respectively. The hottest sites ($\eta > 10^9$) account for just 63 in 1,000,000 of the total but contribute 24% to the overall SERS intensity.

Molecules on nanotextured noble-metal surfaces (1, 2) or nanoparticle aggregates (3, 4) frequently evidence giant Raman scattering cross sections. This surface-enhanced Raman scattering (SERS) effect has enabled a variety of chemical sensing applications (5), including the detection of single molecules by Raman scattering (6, 7). The average value of the Raman enhance-

ment, \bar{G} , is frequently about 10^6 compared with molecules without a SERS substrate. "Hot" spots where the local field enhancement η is 10^9 or more have been detected by searching nanoparticle aggregates with powerful microscopes (6–8). At a hot spot it is possible to measure the Raman spectrum of single molecules (6–8). The existence of hot spots suggests that the average enhancement \bar{G} represents

a broad distribution of microscopic enhancement factors, so a SERS signal might result from a few molecules at hot sites or the preponderance of molecules at "cold" sites (9).

SERS mechanisms may involve electromagnetic enhancement, chemical enhancement, or resonance enhancement. The benzenethiolate (BT) molecule is frequently used as a probe of electromagnetic enhancement. BT forms a densely packed, well-ordered self-assembled monolayer (SAM) on Ag (10) of the type frequently used in chemical sensing measurements. Because BT has weak electronic interactions with metal surfaces and does not absorb at the laser wavelength, the chemical and resonance enhancements are unimportant. In electromagnetic enhancement, an incident laser field, E_{in} , excites surface plasmons to create a complex pattern of spatially varying electromagnetic fields (11, 12). At any location, the local field is gE_{in} , where g is the local enhancement factor. For the purposes of this study, it is sufficient to use the approximation (13) that

School of Chemical Sciences, University of Illinois at Urbana-Champaign, Urbana, IL 61801, USA.

*These authors contributed equally to this work.

†To whom correspondence should be addressed. E-mail: dlott@scs.uiuc.edu

This copy is for your personal, non-commercial use only.

If you wish to distribute this article to others, you can order high-quality copies for your colleagues, clients, or customers by [clicking here](#).

Permission to republish or repurpose articles or portions of articles can be obtained by following the guidelines [here](#).

The following resources related to this article are available online at www.sciencemag.org (this information is current as of September 21, 2015):

Updated information and services, including high-resolution figures, can be found in the online version of this article at:

<http://www.sciencemag.org/content/321/5887/385.full.html>

Supporting Online Material can be found at:

<http://www.sciencemag.org/content/suppl/2008/07/17/321.5887.385.DC1.html>

This article **cites 26 articles**, 5 of which can be accessed free:

<http://www.sciencemag.org/content/321/5887/385.full.html#ref-list-1>

This article has been **cited by** 232 article(s) on the ISI Web of Science

This article has been **cited by** 53 articles hosted by HighWire Press; see:

<http://www.sciencemag.org/content/321/5887/385.full.html#related-urls>

This article appears in the following **subject collections**:

Materials Science

http://www.sciencemag.org/cgi/collection/mat_sci